HHS Public Access

Author manuscript

J Alzheimers Dis. Author manuscript; available in PMC 2022 August 17.

Published in final edited form as:

J Alzheimers Dis. 2022 ; 88(2): 693–705. doi:10.3233/JAD-220335.

Pattern of Altered Magnetization Transfer Rate in Alzheimer's Disease

Wenna Duan, PhD[a], **Parshant Sehrawat, MS**[a], **Tony D. Zhou**[b], **James T. Becker, PhD**[c,d], **Oscar L. Lopez, MD**[d], **H. Michael Gach, PhD**[b], **Weiying Dai, PhD**[a]

[a]Department of Computer Science, State University of New York at Binghamton, Binghamton, NY

[b]Departments of Radiation Oncology, Radiology, and Biomedical Engineering, Washington University in St. Louis, Saint Louis, MO

[c]Department of Psychology, University of Pittsburgh, Pittsburgh, PA

[d]Department of Psychiatry and Neurology, University of Pittsburgh, Pittsburgh, PA

Abstract

Background: Biomarkers for Alzheimer's disease (AD) are crucial for early diagnosis and treatment monitoring once disease modifying therapies become available.

Objective: This study aims to quantify the forward magnetization transfer rate (k_{for}) map from brain tissue water to macromolecular protons and use it to identify the brain regions with abnormal k_{for} in AD and AD progression.

Methods: From the Cardiovascular Health Study (CHS) cognition study, magnetization transfer imaging (MTI) was acquired at baseline from 63 participants, including 20 normal controls (NC), 18 with mild cognitive impairment (MCI), and 25 AD subjects. Of those, 53 participants completed a follow-up MRI scan and were divided into four groups: 15 stable NC, 12 NC-to-MCI, 12 stable MCI, and 14 MCI/AD-to-AD subjects. k_{for} maps were compared across NC, MCI, and AD groups at baseline for the cross-sectional study and across four longitudinal groups for the longitudinal study.

RESULTS: We found a lower k_{for} in the frontal gray matter (GM), parietal GM, frontal corona radiata (CR) white matter (WM) tracts, frontal and parietal superior longitudinal fasciculus (SLF) WM tracts in AD relative to both NC and MCI. Further, we observed progressive decreases of k_{for} in the frontal GM, parietal GM, frontal and parietal CR WM tracts, and parietal SLF WM tracts in stable MCI. In the parietal GM, parietal CR WM tracts, and parietal SLF WM tracts, we found trend differences between MCI/AD-to-AD and stable NC.

Correspondence to: Weiying Dai, Binghamton University, 4400 Vestal Pkwy E, Binghamton, NY, 13902 USA, Phone: (607) 777-4859, wdai@binghamton.edu, H. Michael Gach, Washington University in St. Louis, 4921 Parkview Place, Saint Louis, MO, 63110, Phone: (314)-286-1645, gachhm@wustl.edu.

Disclaimer

The content is solely the responsibility of the authors and does not necessarily represent the official views of the National Institutes of Health and National Science Foundation.

Conflict of Interest

The authors have no conflict of interest to report.

CONCLUSION: Forward magnetization transfer rate is a promising biomarker for AD diagnosis and progression.

Keywords

Alzheimer's disease; mild cognitive impairment; magnetization transfer imaging; magnetization transfer rate

INTRODUCTION

Alzheimer's disease (AD) is the most common cause of dementia in older adults and mild cognitive impairment (MCI) is often considered as a transitional clinical phase between normal brain aging and AD [1]. Brain magnetic resonance imaging (MRI) studies have shown that AD involves abnormalities in both gray matter (GM) and white matter (WM). Structural MRI demonstrated the discriminative and predictive power of atrophy in the hippocampus and entorhinal cortex and ventricular enlargement [2–4]. Perfusion MRI detected compromised cerebral blood flow in the posterior cingulate, precuneus, parietal, hippocampus, temporal, and frontal regions [5, 6]. Diffusion tensor imaging (DTI) assessed brain microstructural changes and reported integrity disruption of WM pathways in corona radiata, superior and inferior longitudinal fasciculus, corpus callosum for individuals with preclinical AD, such as those with subjective cognitive decline [7], positive amyloid β protein levels [8], and clinically diagnosed AD [9–11].

Magnetization transfer imaging (MTI) evaluates brain microstructure in both GM and WM and has been used in the detection of AD. MTI includes the techniques of chemical exchange saturation transfer (CEST), $T_1\rho$, and magnetization transfer (MT) weighted MRI [12, 13]. MT results from dipolar coupling and ^1H exchange between tissue water and macromolecular proton compartments [14]. Macromolecules like proteins cannot be imaged with conventional MRI due to their very short T_2 values [15]. However, macromolecules can be interrogated through their interaction with tissue water. For example, the off-resonance RF excitation of the macromolecular protons changes the relaxation times and magnetization in the tissue water proton pool. The magnetization transfer ratio (MTR) can be derived from water proton images with and without off-resonance RF saturation and it was associated with axonal attenuation and myelin content [16–18]. MTR is reduced in AD in the whole brain [19–21], GM [20, 22], WM [22], hippocampus [19, 23, 24], and medial temporal lobes [20]. However, in order to increase the reliability of the measurements, MTR was exclusively assessed in specific regions of interest. This means that the investigators may have excluded regions for analysis in order to optimize power in the other regions. In addition, MTR is affected by the RF excitation amplitude, frequency offset, duty cycle, the acquisition parameters, and tissue properties. Therefore, it is preferable to measure voxel-level MT-related intrinsic tissue properties, e.g., the forward magnetization transfer rate (k_{for}) map from tissue water to macromolecular protons, that are independent of the details of the data acquisition [25].

In this study, we developed a method to quantify the k_{for} map on a voxel-by-voxel basis and assessed the sensitivity of the k_{for} map in AD diagnosis and progression without a

priori hypotheses regarding which regions would be affected in both the cross-sectional and longitudinal analyses. The MTI data were acquired to measure tissue T_1 when the arterial spin labeling pulse sequence was applied on upstream blood vessels [26–28]. Preliminary results of MT effects of the arterial spin labeling sequence were reported [29]. The resulting k_{for} was used to investigate the extent of microstructural damage of brain GM and WM regions from the entire AD progression spectrum: normal controls (NC), MCI, and AD.

METHOD

Theory

The T_1 value observed in the brain after macromolecular saturation (T_{1sat}) can be modeled as [30–32]:

$$\frac{1}{T_{1sat}} = \frac{1}{T_{1t}} + \frac{f}{\lambda} + k_{for} \quad [1]$$

where T_{1t} is the T_1 of brain tissue water protons, f is the perfusion in ml/(100 g·s), λ is the brain-blood partition coefficient (typically 0.9 ml blood/g brain tissue) [33], k_{for} is the forward magnetization transfer rate for tissue to macromolecular water protons, and is a measure of tissue health. It is worth noting that Eq. [1] is true only when the macromolecular pool is fully saturated.

The T_1 value without macromolecular saturation (T_{1nosat}) is given by [31, 32]:

$$\frac{1}{T_{1nosat}} = \frac{1}{T_{1t}} + \frac{f}{\lambda} \quad [2]$$

k_{for} can be derived from the subtraction of Eq. [2] from Eq. [1] as:

$$k_{for} = \frac{1}{T_{1sat}} - \frac{1}{T_{1nosat}} \quad [3]$$

Participants

From 2002–2013, the Cardiovascular Health Study Cognition Study (CHS-CS) [34] measured cerebral blood flow, brain morphology and tissue health in 195 elderly volunteers at baseline. During the study, the volunteers progressed from normal cognition (NC) to mild cognitive impairment (MCI) and AD. Volunteers received follow-up MRIs during the course of the study. The subjects were classified as NC, MCI, or AD based on cognitive status adjudication [34] without verification for deposition of beta-amyloid. The CHS-CS diagnostic criteria for MCI in the study included both MCI-amnestic type and MCI-multiple cognitive domain type [34]. Sixty-three age matched elderly volunteers from the CHS-CS study, including 20 NC (mean age ± SD, 84.40 ± 4.38 years), 18 MCI (mean age ± SD, 84.77 ± 3.01 years) and 25 early AD (mean age ± SD, 84.40 ± 3.30 years) were scanned using MRI to measure MT effects at baseline. Of those, 53 participants completed a follow-up MRI scan to measure the same MT effects as the baseline. The longitudinal follow-up scans can be divided into four groups: 15 stable NC (follow-up time ± SD: 2.75 ± 1.90

years), 12 NC-to-MCI (follow-up time ± SD: 3.08 ± 2.20 years), 12 stable MCI (follow-up time ± SD: 2.69 ± 1.81 years), and 14 MCI/AD-to-AD (follow-up time ± SD: 1.91 ± 1.37 years) subjects. Modified Mini-Mental State Examination (3MSE) scores [35] were used to assess general cognitive ability for the population. It has been shown that 3MSE scores have increased sensitivity in detecting dementia in comparison to the Mini-Mental State Examination (MMSE) [36, 37].

MRI Protocol

All MRIs were performed on a dedicated GE Signa 1.5 T MRI (Version LX) at the University of Pittsburgh MR Research Center after informed consent. An inversion recovery sequence was performed with or without off-resonance macromolecular saturation. The images were acquired using multi-slice echo planar imaging (EPI) (field of view = 24 × 24 cm, matrix = 64 × 64, 19 slices, Thickness/Spacing: 5/0 mm, TE/TR: 21/9000 ms, 90°, 977 Hz/pixel) with twelve inversion times (TIs) for the first slice from: 0.025, 0.11, 0.195, 0.28, 0.365, 0.535, 0.705, 0.875, 1.3, 1.725, 2.15, and 2.575s (sample sets of 12 TI images without and with off-resonance saturation are shown in Fig. 1A and Fig. 1B). Images were acquired using a quadrature transceiver RF coil. The 19 slices were acquired sequentially from superior to inferior during a 1 s multi-slice acquisition. Therefore, TIs varied slice by slice. The off-resonance macromolecular saturation was administered between the inversion pulse and the image acquisition, using a pulse train with an input amplitude of 3.5 μT at 92% duty cycle and 85 ms repetition time and a frequency offset of 10.6 kHz below the water frequency. This frequency offset, originally designed to measure the MT effects of the continuous arterial spin labeling (CASL) sequence, is therefore larger than the 1–3 kHz frequency offset in typical MTI [38–41]. T_1 maps were quantified from the images acquired with and without macromolecular saturation, referred to as T_{1sat} and T_{1nosat} maps respectively.

Coronal T_1-weighted three-dimensional anatomical images were acquired with spoiled gradient-echo (SPGR) images (field of view = 24 × 19 cm, matrix = 256 × 192, TE/TR = 5/25 ms, flip angle = 40°, slice thickness/gap = 1.5/0 mm, number of slices = 124, bandwidth = 63 Hz/pixel).

Image Analysis

Calculation of T_{1sat} and T_{1nosat}—To correct for the subject motion, SPM12 “realign” was used to align all of the 12 images acquired with and without off-resonance saturation. In principle, T_{1sat} at each single voxel can be calculated by fitting the inversion recovery signals as a function of the TIs.

$$s(TI) = P\left(1 - 2e^{-TI/T_{1sat}}\right) \quad [4]$$

where TI is the inversion time, s(TI) is the signal at inversion time TI, P is the proton density, and T_{1sat} is the T_1 value measured after the application of off-resonance RF pulse. Eq. [4] represents a two-parameter fit that may assume perfect inversion that is unrealistic when the B_1 field is inhomogeneous. However, combining the Eq. [4] with the

signal-weighted inversion time (see Eq. [5]) one can calculate T_{1sat} numerically, resulting in better results than a nominal three-parameter fit.

The signal-weighted inversion time is calculated as below.

$$WI(T_{1sat}) = \frac{\sum_{i=1}^{12} TI_i \quad s(TI_i)}{\sum_{i=1}^{12} s(TI_i)} \qquad [5]$$

This simple first moment noniterative algorithm proved to be very robust. The signal-weighted inversion time, WI, was numerically calculated using Eq. [4] for a range of T_{1sat}. WI was found to be a function consisting of two monotonic functions of T_{1sat} with a singular point T_{1max}, as shown in Fig. 2A. These two monotonic curves can be reorganized to form a single monotonic curve (Fig. 2B), which could be numerically inverted to calculate T_{1sat} from WI. T_{1nosat} was calculated using the same method as T_{1sat} but with the signal images acquired without macromolecular saturation. Sample images of T_{1nosat} and T_{1sat} are shown in Fig. 1C and Fig. 1D.

Calculation of k_{for}—The realigned 12 image sets with and without macromolecular saturation were averaged to calculate mean images, respectively. For each subject, the mean realigned image with macromolecular saturation was co-registered to the mean realigned image without saturation and the co-registration parameters were used to transform the T_{1sat} map to align with the T_{1nosat} map. k_{for} was calculated from the aligned T_{1sat} and T_{1nosat} maps using Eq. [3]. To eliminate extreme values in these k_{for} maps, the signal less than −0.1 and greater than 0.6 was assigned to −0.1 and 0.6, respectively. Although k_{for} should not be negative in general, those negative values were left in k_{for} maps to avoid violating noise distribution. Sample images of T_{1nosat} - T_{1sat} and k_{for} are shown in Fig. 1E and Fig. 1F. The large frequency offset in the pulse sequence cannot fully saturate the macromolecular pool, and therefore the measured k_{for} will be underestimated.

Normalization of T_{1sat}, T_{1nosat}, and k_{for} maps—Anatomical SPGR images were segmented into GM, WM, and cerebrospinal fluid (CSF) probability maps using SPM12's "segment" tool. The GM probability map was co-registered to the mean realigned image without saturation so the transformed GM probability map were aligned with T_{1sat}, T_{1nosat}, and k_{for} maps. The transformed GM probability map was registered to the GM template in the standard MNI brain, and the warping parameters were used to transform the T_{1sat}, T_{1nosat}, and k_{for} maps to the standard MNI brain space.

Statistical Analysis

Demographic and neuropsychological data were analyzed with MATLAB, version R2019a. All tests were 2-tailed and the significance was set for $p < 0.05$. Normality was assessed with the Shapiro-Wilk test. Demographic and neuropsychological characteristics for the NCs, MCIs, ADs at baseline and for stable-NCs, NC-to-MCIs, stable-MCIs and MCI/AD-to-ADs at follow-up were compared using either two-sample t-tests (for normal distribution) or Mann-Whitney nonparametric U-tests (for non-normal distribution) for continuous variables and χ^2 test for categorical variables.

Generation of global regions of interest (ROIs) (whole brain, GM, and WM)—The global ROIs (whole brain, GM, and WM) were obtained by thresholding the corresponding SPM a priori probability map in the standard space with probability greater than 0.3, 0.8, and 0.95, respectively. The selected threshold levels allow us to minimize partial volume effects and have a sufficient number of voxels for reliable averaging. Regional k_{for} values were calculated as the median over each brain global ROI.

Voxel-level analysis on k_{for} maps at baseline—k_{for} maps were compared voxel-by-voxel among the three baseline groups using SPM's general linear model (GLM), controlling for age and gender. Because of partial coverage, only the voxels in which k_{for} maps had valid values (intersection area from both T_{1sat} and T_{1nosat} maps) from all the participants were analyzed. The analyzed area in the SPM analysis is shown in Supplement 1A. A voxel-level p-value of 0.01 was used to threshold the statistical maps. A cluster-level p-value of 0.05 was used to guard against false positives from multiple comparisons. The MCI and AD-affected regions were used for further region-based analyses.

Voxel-level analyses on longitudinal changes of k_{for}—The longitudinal changes of k_{for} were compared among the stable-NCs, NC-to-MCIs, stable-MCIs and MCI/AD-to-ADs using a multiple linear regression. The longitudinal change of k_{for} maps for each subject was calculated between the baseline and follow-up scans and compared voxel-by-voxel among the four longitudinal groups using SPM's GLM, controlling for age, gender and years between baseline and follow-up scans. The analyzed area in the SPM analysis is shown in Supplement 1B. A voxel-level p-value of 0.01 was used to threshold the statistical maps. A cluster-level p-value of 0.05 was used to guard against false positives from multiple comparisons. A more liberal voxel-level threshold of $p < 0.025$ was used to view the trends of longitudinal changes, although a corrected cluster-level threshold of $p < 0.05$ was still used for comparisons.

Region-level analyses on longitudinal changes of k_{for}—Regional k_{for} comparisons were performed among the four longitudinal groups for the whole brain, GM, WM, and MCI/AD-affected regions detected in the voxel-level cross-sectional analysis, controlling for age, gender and follow-up time between baseline and follow-up scans. Post hoc regional analyses were also performed to determine whether the regions detected in the voxel-level longitudinal analysis had better sensitivity in group differences.

RESULTS

Demographic and cognitive Information

Table 1 summarizes the subjects' demographic and cognitive data for the cross-sectional and longitudinal analyses. For the cross-sectional analysis, no significant difference was found for age and gender across the NC, MCI, and AD groups. The AD group showed significantly lower 3MSE scores than the NC and MCI groups. For the longitudinal analysis, no significant difference was found for age, gender, follow-up time, and changes in 3MSE scores across the stable-NC, NC-to-MCI, stable-MCI, and MCI/AD-to-AD groups. The

MCI/AD-to-AD group showed significantly lower 3MSE scores at baseline compared to the stable-NC, NC-to-MCI and stable-MCI groups.

Cross-sectional comparisons of T_{1nosat}, T_{1sat}, and k_{for} in the global ROIs

T_{1nosat} values were not significantly different in the whole brain (561 ± 119 ms), GM (957 ± 246 ms), and WM (688 ± 133 ms) among the NC, MCI and AD groups. T_{1sat} values were significantly higher in WM for ADs vs. NCs ($p = 0.0061$; 672 ± 158 ms vs. 556 ± 92 ms) and for ADs vs. MCIs ($p = 0.022$; 672 ± 158 ms vs. 560 ± 142 ms), but not different for whole brain (529 ± 97 ms) and GM (978 ± 247 ms) among the NC, MCI and AD groups. k_{for} values were significantly lower in WM for ADs vs. NCs ($p = 0.0049$; 0.17 ± 0.16/s vs. 0.35 ± 0.23/s) and for ADs vs. MCIs ($p = 0.00087$; 0.17 ± 0.16/s vs. 0.36 ± 0.17/s) and in the whole brain for ADs vs. MCIs ($p = 0.0041$; 0.16 ± 0.11/s vs. 0.27 ± 0.11/s), but not different for GM (0.065 ± 0.036/s) among the NC, MCI and AD groups.

Cross-sectional voxel-wise group comparisons

Example k_{for} maps from each group of NC, MCI, and AD subjects are shown in Fig. 3. Compared to the NC group, the AD group had significantly decreased k_{for} in three clusters: the left corona radiata WM region (cluster 1, in green circle, $p = 0.044$), right corona radiata extending to superior longitudinal fasciculus WM regions and right frontal lobe extending to precentral GM regions (cluster 2, in purple circle, $p = 0.001$) (Fig. 4A), and the right superior longitudinal fasciculus WM region and right postcentral, paracentral lobule and precuneus GM regions (cluster 3, $p = 0.031$) (Fig. 4B).

Compared to the MCI group, the AD group had significantly decreased k_{for} in two clusters: the left corona radiata, internal capsule, external capsule and corpus callosum WM region and left cingulum, putamen, precentral, insula, and superior medial frontal GM regions (cluster 4, in green circle, $p < 0.001$), and the right corona radiata, external capsule, superior longitudinal fasciculus and internal capsule WM regions and putamen, insula, middle frontal, and right superior frontal GM regions (cluster 5, in purple circle, $p < 0.001$) (Fig. 4C). Statistics of the clusters are listed in Table 2.

Longitudinal voxel-wise group comparisons

Compared to the stable-NC group, the stable-MCI group exhibited larger k_{for} decreases in the left corona radiata extending to the left superior longitudinal fasciculus WM regions (cluster 6, in green circle, $p = 0.003$) and the right corona radiata and right superior frontal GM regions (cluster 7, in purple circle, $p = 0.017$) (Fig. 5A–5B). No significant changes were observed for the other longitudinal groups for voxel-level p-value of 0.01. With less stringent voxel-level p-value of 0.025, compared to the stable-NC group, a symmetrical k_{for} decrease pattern of left and right sides was observed in the stable-MCI group (Supplementary Fig. 2); the MCI/AD-to-AD group exhibited a larger trend of k_{for} decreases in the corpus callosum, right superior longitudinal fasciculus, right corona radiata and cingulum WM regions and the left precuneus, posterior cingulate and left inferior parietal GM regions (cluster 8, $p = 0.012$) (Fig. 5C). Statistics of the clusters are listed in Table 3.

Longitudinal regional group comparisons

Longitudinal k_{for} decreases were observed significantly different from zero ($p < 0.001$) on the global ROIs and the clusters 1–5 derived from the cross-sectional study. However, compared to the changes in the stable NC group, longitudinal k_{for} changes in the other groups were found only marginally different on the global ROIs and the cross-sectional clusters. Specifically, compared to the stable NC group, the stable MCI group exhibited marginally larger longitudinal k_{for} decreases in the whole brain ($p = 0.068$), cluster 2 ($p = 0.080$), and cluster 5 ($p = 0.072$). The MCI/AD-to-AD group had marginally larger longitudinal k_{for} decreases in the WM ($p = 0.062$), cluster 1 ($p = 0.058$), cluster 2 ($p = 0.083$) and cluster 5 ($p = 0.085$).

The regional k_{for} values in the clusters derived from the longitudinal voxel-wise analyses corroborated the voxel-level results and exhibited more significant changes. We used larger and symmetrical clusters 6–7 (voxel-level p value of 0.025) for the regional analyses. In cluster 6, significantly larger longitudinal k_{for} decreases were observed in the NC-to-MCI, stable MCI and MCI/AD-to-AD groups (Fig. 6, $p = 0.05$, $p = 0.0006$, and $p = 0.0115$ respectively) when compared to the stable NC group. In clusters 7 and 8, compared to the stable NC group, significantly larger longitudinal k_{for} decreases were observed only in the stable MCI group (Fig. 6, $p = 0.0010$ and $p = 0.0078$ for the clusters 7 and 8, respectively) and the MCI/AD-to-AD groups (Fig. 6, $p = 0.0129$ and $p = 0.0008$ for the clusters 7 and 8, respectively), while marginally larger longitudinal k_{for} decreases were observed in the NC-to-MCI group (Fig. 6, $p = 0.0796$ and $p = 0.0719$ for the clusters 7 and 8, respectively). Years between baseline and follow-up scans were significantly associated with the longitudinal changes in k_{for} ($p < 0.05$).

DISCUSSION

We found lower k_{for} in the frontal GM, parietal GM, frontal corona radiata WM tracts, frontal and parietal superior longitudinal fasciculus WM tracts in ADs relative to both NCs and MCIs. From the longitudinal study, we also observed progressive decreases in k_{for} in the frontal GM, parietal GM, frontal and parietal corona radiata WM tracts, and parietal superior longitudinal fasciculus WM tracts in stable MCIs; and in the parietal GM, parietal corona radiata WM tracts, and parietal superior longitudinal fasciculus WM tracts in MCI/AD-to-ADs.

Lower k_{for} values were previously reported in the hippocampus, temporal lobe, posterior cingulate cortex, and parietal GM regions [42] and preselected WM fiber tracts [43] of AD patients. Lower k_{for} values in the WM tract were reported to differentiate MCI converters from stable MCIs [43]. Other quantitative MT parameters, such as the T_2 of the restricted pool, fractional pool size, and the ratio of relaxation times of the free proton pool to restricted pool, were associated with AD [44, 45]. However, these quantitative MT parameters were mostly analyzed on predetermined regions of interest for increased signal-to-noise ratio. Our study explored voxel-wise k_{for} abnormalities in AD and AD progression and allowed accurate detection for abnormal k_{for} spatial locations related to AD without a priori hypotheses.

The detected abnormal k_{for} GM regions included the superior frontal GM, anterior cingulate, inferior parietal, posterior cingulate, and precuneus regions. These regions are consistent with regions with reduced cerebral blood flow [26, 27] and reduced glucose metabolism [46, 47] that are typically reported in AD. Due to its overlap with regions with blood flow and metabolic deficits, this finding supports that k_{for} is related to metabolic processes [48] and mitochondrial dysfunction may play a role in the pathophysiology of AD for GM damage [49]. N-acetylaspartate (NAA), a neuron-specific metabolite synthesized by the mitochondria, has been reported with significant reduction in the whole brain tissue of MCI patients [50]. The reduction of NAA in the MCI further supports energy impairment and mitochondrial dysfunction may be already evident before individuals are clinically demented [50, 51]. Energy impairment from mitochondrial dysfunction causes neuronal and axonal damage, and therefore reduces magnetization transfer effects. The abnormal k_{for} WM regions included the frontal and parietal corona radiata, and superior longitudinal fasciculus. Reduced k_{for} values in WM tracts of AD patients have been correlated to smaller fractional anisotropy values using DTI [43], which can be influenced by demyelination. Mitochondrial dysfunction was found to contribute to WM demyelination in multiple sclerosis [52, 53]. Therefore, mitochondrial dysfunction may play a similar role in the pathophysiology of AD for WM damage. Although highly speculative, our study supports a uniform role of mitochondrial dysfunction in the pathophysiology of AD.

We also observed k_{for} decreases in the whole brain and global WM in ADs relative to MCIs or NCs and longitudinal decreases of k_{for} in the whole brain and global WM in ADs and MCIs. Existing studies using MTR mostly focused on histogram analyses in large regions [19, 21, 22, 54, 55], such as the whole brain, GM, WM, and some hypothesized regions, such as hippocampal regions and deep GM regions. Our study supports the whole brain and global WM microstructure deficits in AD. An MTR study analyzed the frontal lobe and found reduced histogram properties in the region [21]. Therefore, our findings extend current microstructural deficits of AD to the frontal WM and parietal WM, and also specify the deficits in two WM tracts.

Only one longitudinal MTR study was found and it reported that AD patients had significant longitudinal decreases of MTR in the whole brain and all deep GM regions that were investigated over 12 months [55]. We extended these findings by demonstrating that the longitudinal decreases in k_{for} are significantly larger in stable MCIs and MCI/AD-to-ADs than in stable NCs, indicating that AD pathology accelerates k_{for} declines in frontal and parietal GM regions and WM tracts.

The frontal and parietal WM deficits in k_{for} are also in line with the locations for WM microvascular damage observed with mean diffusivity and fractional anisotropy using DTI [56–58]. Altered mean diffusivity and free water signal fraction in the frontal WM and temporal WM regions have been significantly correlated with CSF biomarkers in AD [58]. We did not observe deficits in the k_{for} of the temporal region. However, the temporal region was located in the inferior portion of the imaging volume and only the overlapped regions covered across the subjects were analyzed. It is worth noting that anterior (frontal) corona radiata and posterior (parietal) corona radiata were listed as clusters with significant association with k_{for} declines. A DTI meta-analysis showed significant decreases of both

WM volume and fractional anisotropy in corona radiata in ADs [10]. The alterations from both corona radiata and superior longitudinal fasciculus WM tracts were also supported by longitudinal DTI analysis in AD [11, 59].

Years between baseline and follow-up scans were significantly associated with the longitudinal changes in k_{for}. Our results support the involvement of frontal and parietal GM regions and WM tracts (corona radiata and superior longitudinal fasciculus) in the progression of AD, highlighting MTRs of those regions as promising biomarkers and disconnection of fibers as a potential mechanism.

This study has limitations, the most important of which is a consequence of the technical aspects of scanning and measuring magnetization transfer. Specifically, the data becomes less reliable in the more ventral aspects of the brain. in addition, we set the stringent criterion that each voxel must have representation from every subject in order to be included in the analyses. Therefore, the more ventral regions of the brain, most importantly including the inferior and middle temporal gyri, and the mesial temporal lobe including the hippocampus, were not included in the analyses. Consequently, there may be important, subtle changes in MTR in these regions, especially in the transition from normal cognition to MCI. For future studies we will need more focused protocols in order to examine these brain regions, but critically, we have derived a measure of magnetization transfer rate from a data set that was not designed for this purpose.

Second, the images acquired with and without macromolecular saturation were acquired at 1.5 T before the widespread availability of 3 T. We expect that MTI studies at 3 T can benefit from longer T1 relaxation times in addition to higher steady state magnetization. However, the method of continuous off-resonance saturation used in this study would probably not be practical at 3 T due its high specific absorption rate (SAR). Nevertheless, we were able to observe the k_{for} differences between NCs, MCIs, and ADs at 1.5 T.

Third, we had small sample sizes, especially for the longitudinal analysis. This limits the statistical power to detect longitudinal changes for the groups with large variations. The fourth longitudinal group was a combined group from the subjects who turned into AD from MCI stage and those who stayed in the AD stage, resulting from the small numbers of participants in these two categories. If repeated in a larger population, there is a potential for a better understanding of the full trajectory of disease progression using k_{for}.

Fourth, no differences were found among the AD progression groups (NC-to-MCI, stable-MCI and MCI/AD-to-AD groups) thus changes in k_{for} during the middle and late stages of AD remain incomplete. The lack of sensitivity may be partially attributed to the reduced sensitivity from the large RF frequency offset used in our protocol. Future studies should evaluate the k_{for} maps using the optimal sequence design (lower RF frequency offset and short RF duration). In addition, the participants were classified into NC, MCI, or AD based on neuropsychological assessments. The lack of neurobiological definition of AD in the study may have mixed subjects with AD pathology (e.g., those with positive beta-amyloid) with those with severe cognitive deficits, leading to reduced sensitivity in k_{for} longitudinal

changes. Unfortunately, neither beta-amyloid nor tau PET imaging was available at the beginning of the CHS-CS.

Fifth, the range of k_{for} is less than 0.6/s, which is on the lower side of the k_{for} ranges from the literature, e.g., 1.35 ± 0.19 /s for a rat study [32] and 0.51 ~ 1.43 /s for a human study [30]. The low k_{for} values result from the large RF frequency offset only partially saturating the macromolecules [60]. Hence, the k_{for} values we presented are relative, not absolute. In addition, the k_{for} values are biased by spatially-dependent B_1 inhomogeneities, inversion times, and off-resonance saturation including excitation crosstalk. 3D acquisitions would eliminate the bias from the slice-dependent inversion times and excitation crosstalk but could exacerbate spatially-dependent B_1 inhomogeneities. Nevertheless, we assumed the systematic bias was consistent between individuals in the group analysis. We were able to observe the k_{for} changes in both cross-sectional and longitudinal studies despite potentially reduced sensitivity associated with these biases.

Sixth, WM hyperintensities were not accounted for in the current analysis. WM hyperintensities are common in older adults with AD subjects having increased WM hyperintensity volume [54, 61]. AD subjects demonstrated decreased MTR in normal-appearing WM and even lower MTR in WM hyperintense regions [54]. Not accounting for WM hyperintensities in this study represents a potential limitation in understanding how different types of WM (normal-appearing WM and hyperintense WM) contributed to reduced k_{for} in AD.

CONCLUSION

Our study reveals that voxel-wise forward magnetization transfer rate maps are efficient in detecting GM and WM microstructural damage in AD diagnosis and AD progression. Future studies are needed to investigate the clinical relevance of k_{for} in posterior cingulate, precuneus, inferior parietal, anterior cingulate, and superior frontal GM regions and corona radiata and superior longitudinal fasciculus WM tracts.

Supplementary Material

Refer to Web version on PubMed Central for supplementary material.

Acknowledgments

This research was supported by contracts HHSN268201200036C, HHSN268200800007C, HHSN268201800001C, N01HC55222, N01HC85079, N01HC85080, N01HC85081, N01HC85082, N01HC85083, N01HC85086, 75N92021D00006, and grants U01HL080295 and U01HL130114 from the National Heart, Lung, and Blood Institute (NHLBI), with additional contribution from the National Institute of Neurological Disorders and Stroke (NINDS). Additional support was provided by R01AG023629 from the National Institute on Aging (NIA). A full list of principal CHS investigators and institutions can be found at CHS-NHLBI.org. The research was also supported by the State University of New York at Binghamton, the Nevada Cancer Institute, the University of Pittsburgh, and Washington University in St. Louis. Weiying Dai was supported by the National Institute on Aging (NIA) under award number R01AG066430 and the National Science Foundation (NSF) under award number CMMI-2123061. Tony D. Zhou, affiliated with Vestal High School, Vestal, NY, USA, conducted his research under the guidance of Dr. H. Michael Gach.

References

[1]. Petersen RC, Doody R, Kurz A, Mohs RC, Morris JC, Rabins PV, Ritchie K, Rossor M, Thal L, Winblad B (2001) Current concepts in mild cognitive impairment. Arch Neurol 58, 1985–1992. [PubMed: 11735772]

[2]. Ledig C, Schuh A, Guerrero R, Heckemann RA, Rueckert D (2018) Structural brain imaging in Alzheimer's disease and mild cognitive impairment: biomarker analysis and shared morphometry database. Sci Rep 8, 11258. [PubMed: 30050078]

[3]. Vemuri P, Jack CR Jr. (2010) Role of structural MRI in Alzheimer's disease. Alzheimers Res Ther 2, 23. [PubMed: 20807454]

[4]. Chandra A, Dervenoulas G, Politis M, Alzheimer's Disease Neuroimaging I (2019) Magnetic resonance imaging in Alzheimer's disease and mild cognitive impairment. J Neurol 266, 1293–1302. [PubMed: 30120563]

[5]. Alsop DC, Dai W, Grossman M, Detre JA (2010) Arterial spin labeling blood flow MRI: its role in the early characterization of Alzheimer's disease. J Alzheimers Dis 20, 871–880. [PubMed: 20413865]

[6]. Wang Z (2014) Characterizing early Alzheimer's disease and disease progression using hippocampal volume and arterial spin labeling perfusion MRI. J Alzheimers Dis 42 Suppl 4, S495–502. [PubMed: 25182742]

[7]. Brueggen K, Dyrba M, Cardenas-Blanco A, Schneider A, Fliessbach K, Buerger K, Janowitz D, Peters O, Menne F, Priller J, Spruth E, Wiltfang J, Vukovich R, Laske C, Buchmann M, Wagner M, Roske S, Spottke A, Rudolph J, Metzger CD, Kilimann I, Dobisch L, Duzel E, Jessen F, Teipel SJ, Group DS (2019) Structural integrity in subjective cognitive decline, mild cognitive impairment and Alzheimer's disease based on multicenter diffusion tensor imaging. J Neurol 266, 2465–2474. [PubMed: 31227891]

[8]. Molinuevo JL, Ripolles P, Simo M, Llado A, Olives J, Balasa M, Antonell A, Rodriguez-Fornells A, Rami L (2014) White matter changes in preclinical Alzheimer's disease: a magnetic resonance imaging-diffusion tensor imaging study on cognitively normal older people with positive amyloid beta protein 42 levels. Neurobiol Aging 35, 2671–2680. [PubMed: 25002037]

[9]. Mayo CD, Garcia-Barrera MA, Mazerolle EL, Ritchie LJ, Fisk JD, Gawryluk JR, Alzheimer's Disease Neuroimaging I (2018) Relationship between DTI metrics and cognitive function in Alzheimer's disease. Front Aging Neurosci 10, 436. [PubMed: 30687081]

[10]. Yin RH, Tan L, Liu Y, Wang WY, Wang HF, Jiang T, Radua J, Zhang Y, Gao J, Canu E, Migliaccio R, Filippi M, Gorno-Tempini ML, Yu JT (2015) Multimodal voxel-based meta-analysis of white matter abnormalities in Alzheimer's disease. J Alzheimers Dis 47, 495–507. [PubMed: 26401571]

[11]. Mayo CD, Mazerolle EL, Ritchie L, Fisk JD, Gawryluk JR, Alzheimer's Disease Neuroimaging I (2017) Longitudinal changes in microstructural white matter metrics in Alzheimer's disease. Neuroimage Clin 13, 330–338. [PubMed: 28066707]

[12]. van Zijl PC, Yadav NN (2011) Chemical exchange saturation transfer (CEST): what is in a name and what isn't? Magn Reson Med 65, 927–948. [PubMed: 21337419]

[13]. Haris M, Singh A, Cai K, Davatzikos C, Trojanowski JQ, Melhem ER, Clark CM, Borthakur A (2011) T1rho ($T_{1\rho}$) MR imaging in Alzheimer's disease and Parkinson's disease with and without dementia. J Neurol 258, 380–385. [PubMed: 20924593]

[14]. Wolff SD, Balaban RS (1994) Magnetization transfer imaging: practical aspects and clinical applications. Radiology 192, 593–599. [PubMed: 8058919]

[15]. Edzes HT, Samulski ET (1977) Cross relaxation and spin diffusion in the proton NMR or hydrated collagen. Nature 265, 521–523. [PubMed: 834303]

[16]. Schmierer K, Scaravilli F, Altmann DR, Barker GJ, Miller DH (2004) Magnetization transfer ratio and myelin in postmortem multiple sclerosis brain. Ann Neurol 56, 407–415. [PubMed: 15349868]

[17]. Mottershead JP, Schmierer K, Clemence M, Thornton JS, Scaravilli F, Barker GJ, Tofts PS, Newcombe J, Cuzner ML, Ordidge RJ, McDonald WI, Miller DH (2003) High field MRI

correlates of myelin content and axonal density in multiple sclerosis--a post-mortem study of the spinal cord. J Neurol 250, 1293–1301. [PubMed: 14648144]

[18]. Schmierer K, Tozer DJ, Scaravilli F, Altmann DR, Barker GJ, Tofts PS, Miller DH (2007) Quantitative magnetization transfer imaging in postmortem multiple sclerosis brain. J Magn Reson Imaging 26, 41–51. [PubMed: 17659567]

[19]. Ridha BH, Symms MR, Tozer DJ, Stockton KC, Frost C, Siddique MM, Lewis EB, MacManus DG, Boulby PA, Barker GJ, Rossor MN, Fox NC, Tofts PS (2007) Magnetization transfer ratio in Alzheimer disease: comparison with volumetric measurements. AJNR Am J Neuroradiol 28, 965–970. [PubMed: 17494679]

[20]. Bozzali M, Franceschi M, Falini A, Pontesilli S, Cercignani M, Magnani G, Scotti G, Comi G, Filippi M (2001) Quantification of tissue damage in AD using diffusion tensor and magnetization transfer MRI. Neurology 57, 1135–1137. [PubMed: 11571355]

[21]. van der Flier WM, van den Heuvel DM, Weverling-Rijnsburger AW, Bollen EL, Westendorp RG, van Buchem MA, Middelkoop HA (2002) Magnetization transfer imaging in normal aging, mild cognitive impairment, and Alzheimer's disease. Ann Neurol 52, 62–67. [PubMed: 12112048]

[22]. Kabani NJ, Sled JG, Chertkow H (2002) Magnetization transfer ratio in mild cognitive impairment and dementia of Alzheimer's type. Neuroimage 15, 604–610. [PubMed: 11848703]

[23]. Hanyu H, Asano T, Iwamoto T, Takasaki M, Shindo H, Abe K (2000) Magnetization transfer measurements of the hippocampus in patients with Alzheimer's disease, vascular dementia, and other types of dementia. AJNR Am J Neuroradiol 21, 1235–1242. [PubMed: 10954274]

[24]. Hanyu H, Asano T, Sakurai H, Takasaki M, Shindo H, Abe K (2001) Magnetization transfer measurements of the hippocampus in the early diagnosis of Alzheimer's disease. J Neurol Sci 188, 79–84. [PubMed: 11489289]

[25]. Sled JG (2018) Modelling and interpretation of magnetization transfer imaging in the brain. Neuroimage 182, 128–135. [PubMed: 29208570]

[26]. Duan W, Zhou GD, Balachandrasekaran A, Bhumkar AB, Boraste PB, Becker JT, Kuller LH, Lopez OL, Gach HM, Dai W (2021) Cerebral blood flow predicts conversion of mild cognitive impairment into Alzheimer's disease and cognitive decline: an arterial spin labeling follow-up study. J Alzheimers Dis 82, 293–305. [PubMed: 34024834]

[27]. Duan W, Sehrawat P, Balachandrasekaran A, Bhumkar AB, Boraste PB, Becker JT, Kuller LH, Lopez OL, Gach HM, Dai W (2020) Cerebral blood flow is associated with diagnostic class and cognitive decline in Alzheimer's disease. J Alzheimers Dis 76, 1103–1120. [PubMed: 32597803]

[28]. Dai W, Lopez OL, Carmichael OT, Becker JT, Kuller LH, Gach HM (2009) Mild cognitive impairment and alzheimer disease: patterns of altered cerebral blood flow at MR imaging. Radiology 250, 856–866. [PubMed: 19164119]

[29]. Duan W, Sehrawat P, Becker JT, Lopez OL, Gach HM, Dai W (2019) White matter damage of Alzheimer's disease using magnetization transfer imaging. Proceedings of International Society for Magnetic Resonance in Medicine 27, 625.

[30]. Ropele S, Strasser-Fuchs S, Augustin M, Stollberger R, Enzinger C, Hartung HP, Fazekas F (2000) A comparison of magnetization transfer ratio, magnetization transfer rate, and the native relaxation time of water protons related to relapsing-remitting multiple sclerosis. AJNR Am J Neuroradiol 21, 1885–1891. [PubMed: 11110542]

[31]. Silva AC, Zhang W, Williams DS, Koretsky AP (1997) Estimation of water extraction fractions in rat brain using magnetic resonance measurement of perfusion with arterial spin labeling. Magn Reson Med 37, 58–68. [PubMed: 8978633]

[32]. Zhang W, Silva AC, Williams DS, Koretsky AP (1995) NMR measurement of perfusion using arterial spin labeling without saturation of macromolecular spins. Magn Reson Med 33, 370–376. [PubMed: 7760704]

[33]. Herscovitch P, Raichle ME (1985) What is the correct value for the brain-blood partition coefficient for water? J Cereb Blood Flow Metab 5, 65–69. [PubMed: 3871783]

[34]. Lopez OL, Jagust WJ, DeKosky ST, Becker JT, Fitzpatrick A, Dulberg C, Breitner J, Lyketsos C, Jones B, Kawas C, Carlson M, Kuller LH (2003) Prevalence and classification of mild cognitive impairment in the Cardiovascular Health Study Cognition Study: part 1. Arch Neurol 60, 1385–1389. [PubMed: 14568808]

[35]. Teng EL, Chui HC (1987) The Modified Mini-Mental State (3MS) examination. J Clin Psychiatry 48, 314–318. [PubMed: 3611032]

[36]. McDowell I, Kristjansson B, Hill GB, Hebert R (1997) Community screening for dementia: the Mini Mental State Exam (MMSE) and Modified Mini-Mental State Exam (3MS) compared. J Clin Epidemiol 50, 377–383. [PubMed: 9179095]

[37]. Nadler JD, Relkin NR, Cohen MS, Hodder RA, Reingold J, Plum F (1995) Mental status testing in the elderly nursing home population. J Geriatr Psychiatry Neurol 8, 177–183. [PubMed: 7576043]

[38]. Rovaris M, Agosta F, Sormani MP, Inglese M, Martinelli V, Comi G, Filippi M (2003) Conventional and magnetization transfer MRI predictors of clinical multiple sclerosis evolution: a medium-term follow-up study. Brain 126, 2323–2332. [PubMed: 12937086]

[39]. Brex PA, Leary SM, Plant GT, Thompson AJ, Miller DH (2001) Magnetization transfer imaging in patients with clinically isolated syndromes suggestive of multiple sclerosis. AJNR Am J Neuroradiol 22, 947–951. [PubMed: 11337341]

[40]. Foong J, Symms MR, Barker GJ, Maier M, Woermann FG, Miller DH, Ron MA (2001) Neuropathological abnormalities in schizophrenia: evidence from magnetization transfer imaging. Brain 124, 882–892. [PubMed: 11335691]

[41]. Yarnykh VL (2002) Pulsed Z-spectroscopic imaging of cross-relaxation parameters in tissues for human MRI: theory and clinical applications. Magn Reson Med 47, 929–939. [PubMed: 11979572]

[42]. Giulietti G, Bozzali M, Figura V, Spano B, Perri R, Marra C, Lacidogna G, Giubilei F, Caltagirone C, Cercignani M (2012) Quantitative magnetization transfer provides information complementary to grey matter atrophy in Alzheimer's disease brains. Neuroimage 59, 1114–1122. [PubMed: 21983184]

[43]. Makovac E, Serra L, Di Domenico C, Marra C, Caltagirone C, Cercignani M, Bozzali M (2018) Quantitative magnetization transfer of white matter tracts correlates with diffusion tensor imaging indices in predicting the conversion from mild cognitive impairment to Alzheimer's disease. J Alzheimers Dis 63, 561–575. [PubMed: 29689722]

[44]. Kiefer C, Brockhaus L, Cattapan-Ludewig K, Ballinari P, Burren Y, Schroth G, Wiest R (2009) Multi-parametric classification of Alzheimer's disease and mild cognitive impairment: the impact of quantitative magnetization transfer MR imaging. Neuroimage 48, 657–667. [PubMed: 19607926]

[45]. Ridha BH, Tozer DJ, Symms MR, Stockton KC, Lewis EB, Siddique MM, MacManus DG, Rossor MN, Fox NC, Tofts PS (2007) Quantitative magnetization transfer imaging in Alzheimer disease. Radiology 244, 832–837. [PubMed: 17709831]

[46]. Marcus C, Mena E, Subramaniam RM (2014) Brain PET in the diagnosis of Alzheimer's disease. Clin Nucl Med 39, e413–422; quiz e423–416. [PubMed: 25199063]

[47]. Kato T, Inui Y, Nakamura A, Ito K (2016) Brain fluorodeoxyglucose (FDG) PET in dementia. Ageing Res Rev 30, 73–84. [PubMed: 26876244]

[48]. Louie EA, Gochberg DF, Does MD, Damon BM (2009) Transverse relaxation and magnetization transfer in skeletal muscle: effect of pH. Magn Reson Med 61, 560–569. [PubMed: 19097244]

[49]. Moreira PI, Carvalho C, Zhu X, Smith MA, Perry G (2010) Mitochondrial dysfunction is a trigger of Alzheimer's disease pathophysiology. Biochim Biophys Acta 1802, 2–10. [PubMed: 19853658]

[50]. Falini A, Bozzali M, Magnani G, Pero G, Gambini A, Benedetti B, Mossini R, Franceschi M, Comi G, Scotti G, Filippi M (2005) A whole brain MR spectroscopy study from patients with Alzheimer's disease and mild cognitive impairment. Neuroimage 26, 1159–1163. [PubMed: 15878675]

[51]. Signoretti S, Marmarou A, Tavazzi B, Lazzarino G, Beaumont A, Vagnozzi R (2001) N-Acetylaspartate reduction as a measure of injury severity and mitochondrial dysfunction following diffuse traumatic brain injury. J Neurotrauma 18, 977–991. [PubMed: 11686498]

[52]. Witte ME, Mahad DJ, Lassmann H, van Horssen J (2014) Mitochondrial dysfunction contributes to neurodegeneration in multiple sclerosis. Trends Mol Med 20, 179–187. [PubMed: 24369898]

[53]. Carvalho KS (2013) Mitochondrial dysfunction in demyelinating diseases. Semin Pediatr Neurol 20, 194–201. [PubMed: 24331361]

[54]. Colonna I, Koini M, Pirpamer L, Damulina A, Hofer E, Schwingenschuh P, Enzinger C, Schmidt R, Ropele S (2021) Microstructural tissue changes in Alzheimer disease brains: insights from magnetization transfer imaging. AJNR Am J Neuroradiol 42, 688–693. [PubMed: 33509922]

[55]. Ropele S, Schmidt R, Enzinger C, Windisch M, Martinez NP, Fazekas F (2012) Longitudinal magnetization transfer imaging in mild to severe Alzheimer disease. AJNR Am J Neuroradiol 33, 570–575. [PubMed: 22173770]

[56]. Bozzali M, Falini A, Franceschi M, Cercignani M, Zuffi M, Scotti G, Comi G, Filippi M (2002) White matter damage in Alzheimer's disease assessed in vivo using diffusion tensor magnetic resonance imaging. J Neurol Neurosurg Psychiatry 72, 742–746. [PubMed: 12023417]

[57]. Choi SJ, Lim KO, Monteiro I, Reisberg B (2005) Diffusion tensor imaging of frontal white matter microstructure in early Alzheimer's disease: a preliminary study. J Geriatr Psychiatry Neurol 18, 12–19. [PubMed: 15681623]

[58]. Hoy AR, Ly M, Carlsson CM, Okonkwo OC, Zetterberg H, Blennow K, Sager MA, Asthana S, Johnson SC, Alexander AL, Bendlin BB (2017) Microstructural white matter alterations in preclinical Alzheimer's disease detected using free water elimination diffusion tensor imaging. PLoS One 12, e0173982. [PubMed: 28291839]

[59]. Genc S, Steward CE, Malpas CB, Velakoulis D, O'Brien TJ, Desmond PM (2016) Short-term white matter alterations in Alzheimer's disease characterized by diffusion tensor imaging. J Magn Reson Imaging 43, 627–634. [PubMed: 26228096]

[60]. Finelli DA, Reed DR (1998) Flip angle dependence of experimentally determined T1sat and apparent magnetization transfer rate constants. J Magn Reson Imaging 8, 548–553. [PubMed: 9626867]

[61]. Wang YL, Chen W, Cai WJ, Hu H, Xu W, Wang ZT, Cao XP, Tan L, Yu JT, Alzheimer's Disease Neuroimaging I (2020) Associations of White Matter Hyperintensities with Cognitive Decline: A Longitudinal Study. J Alzheimers Dis 73, 759–768. [PubMed: 31839612]

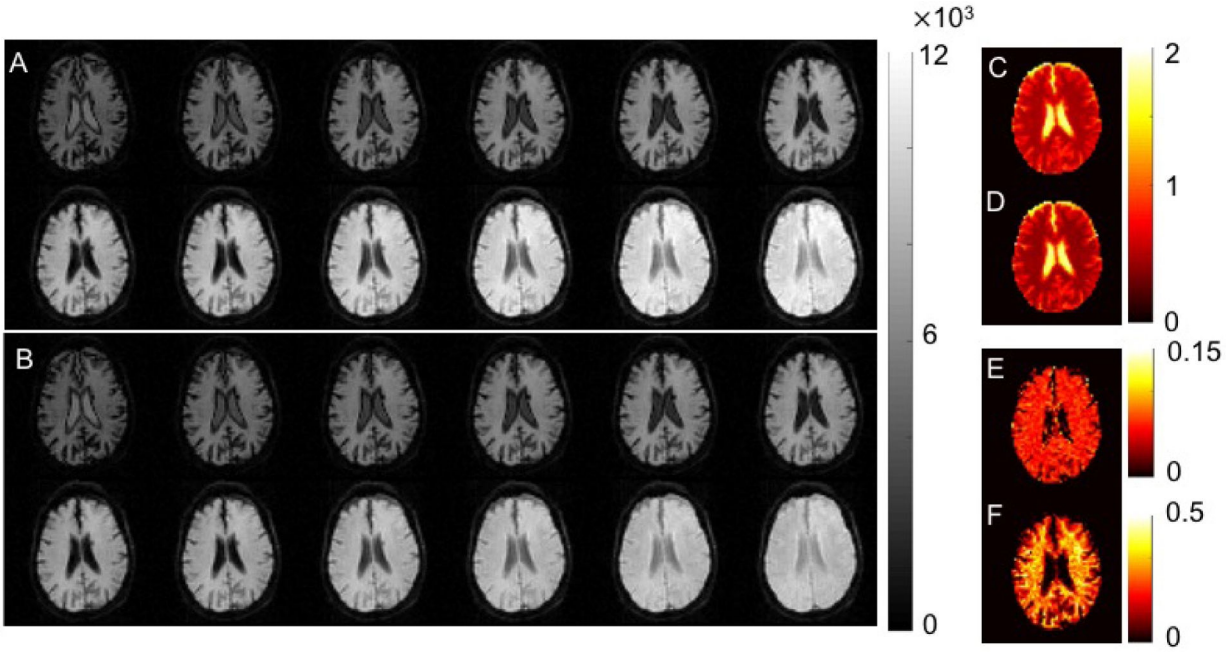

Fig. 1.

Sample images from a middle axial slice of a normal control subject. (A) 12 TI images of T_{1nosat}, (B) 12 TI images of T_{1sat}, (C) T_{1nosat} image derived from (A), (D) T_{1sat} image derived from (B), (E) $T_{1nosat} - T_{1sat}$ image, and (F) k_{for} image. The 12 TIs for the slice were 0.499, 0.584, 0.669, 0.754, 0.839, 1.009, 1.179, 1.349, 1.774, 2.199, 2.624, and 3.049s, respectively.

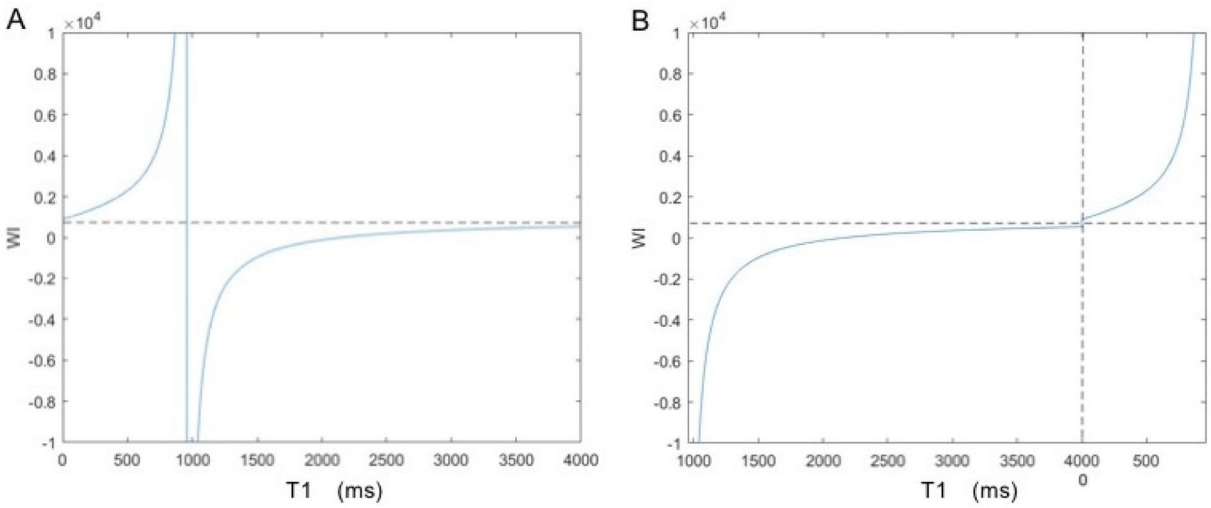

Fig. 2.

Numerical calculation of T_1 (T_{1sat} and T_{1nosat}) using signal weighted inversion (WI). (A) Theoretical graph of WI as a function of T_1 (Equation [5], with T_{1sat} replaced by T_1 for generality), WI reaches its maximum value at T_{1max}, (B) WI forms a monotonically increasing curve of T_1 if the curve at [0 T_{1max}] ms is shifted to the right of [T_{1max} 4000] ms. WI is an inversible function except for the values within [WI(4000) WI(0)]. For the value of WI that falls into the range, T1 is assigned to 0 ms or 4000ms depending on whether WI is closer to WI(0) or WI(4000).

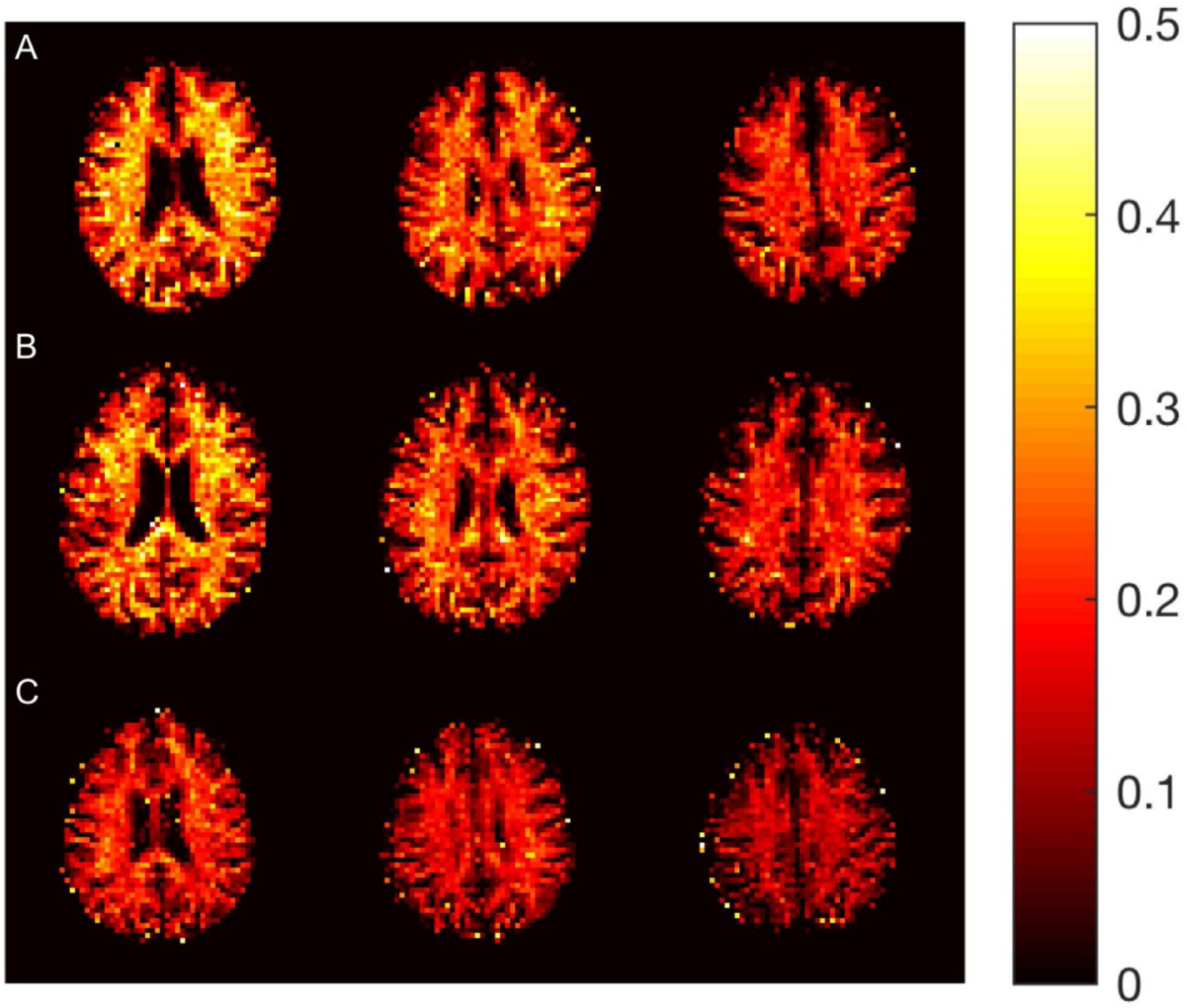

Fig. 3.
Representative k_{for} images from (A) NCs, (B) MCIs, and (C) ADs.

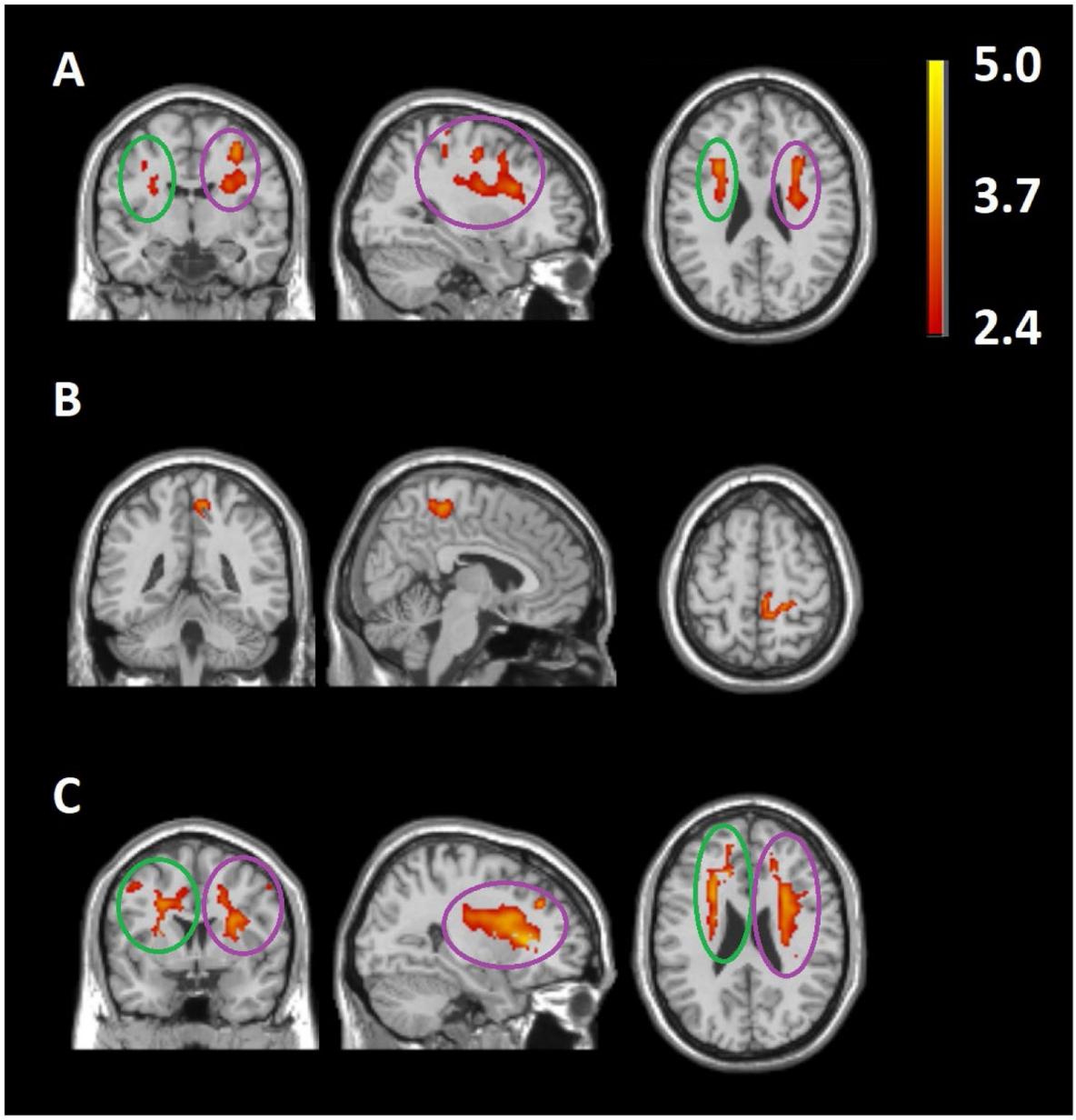

Fig. 4.

Compared to the NC group, the AD group had significantly lower k_{for} values in three clusters: (A) the left corona radiata white matter region (cluster 1 in green circle), right corona radiata extending to superior longitudinal fasciculus white matter regions and right frontal lobe extending to precentral gray matter regions (cluster 2 in purple circle), (B) the right superior longitudinal fasciculus white matter region and at right postcentral, paracentral lobule and precuneus gray matter regions. Compared to the MCI group, the AD group had significantly lower k_{for} values in (C) two clusters: the left corona radiata and internal capsule white matter regions and left anterior cingulum and superior medial frontal gray matter regions (cluster 4 in green circle), and the right corona radiata and external capsule white

matter regions and right superior frontal gray matter regions (cluster 5 in purple circle). The color bar stands for the range of t values.

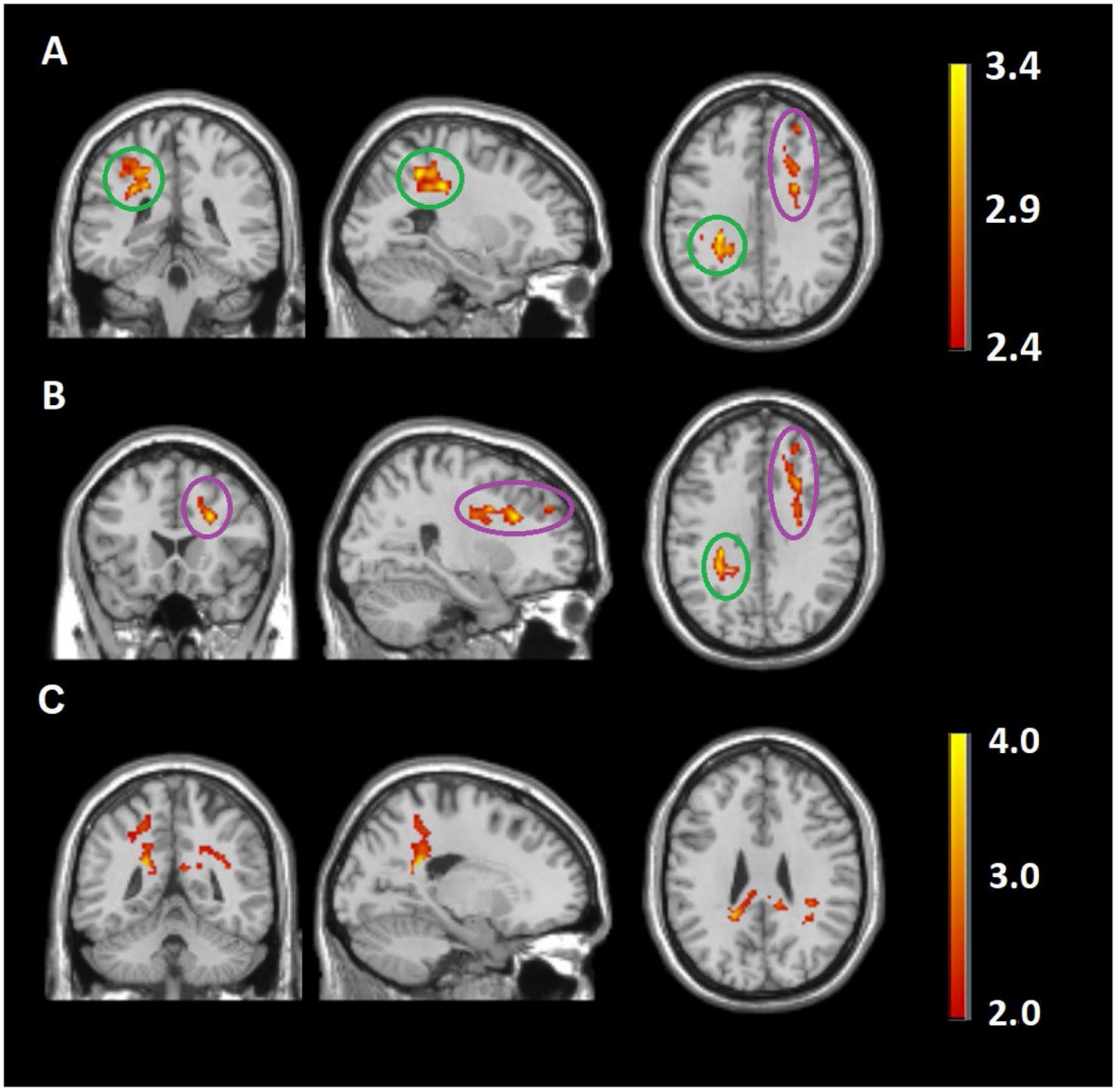

Fig. 5.

Compared to the stable-NC group, the stable-MCI group exhibited larger k_{for} decreases in (A) the left corona radiata extending to left superior longitudinal fasciculus white matter regions (cluster 6, in green circle) and (B) the right corona radiata and right superior frontal gray matter regions (cluster 7, in purple circle). The MCI/AD-to-AD group exhibited larger k_{for} decreases in (C) the corpus callosum, the right superior longitudinal fasciculus, right corona radiate and cingulum white matter regions and the left precuneus, and both sides of the posterior cingulum and left inferior parietal gray matter regions (cluster 8). The color bars stand for the range of t values.

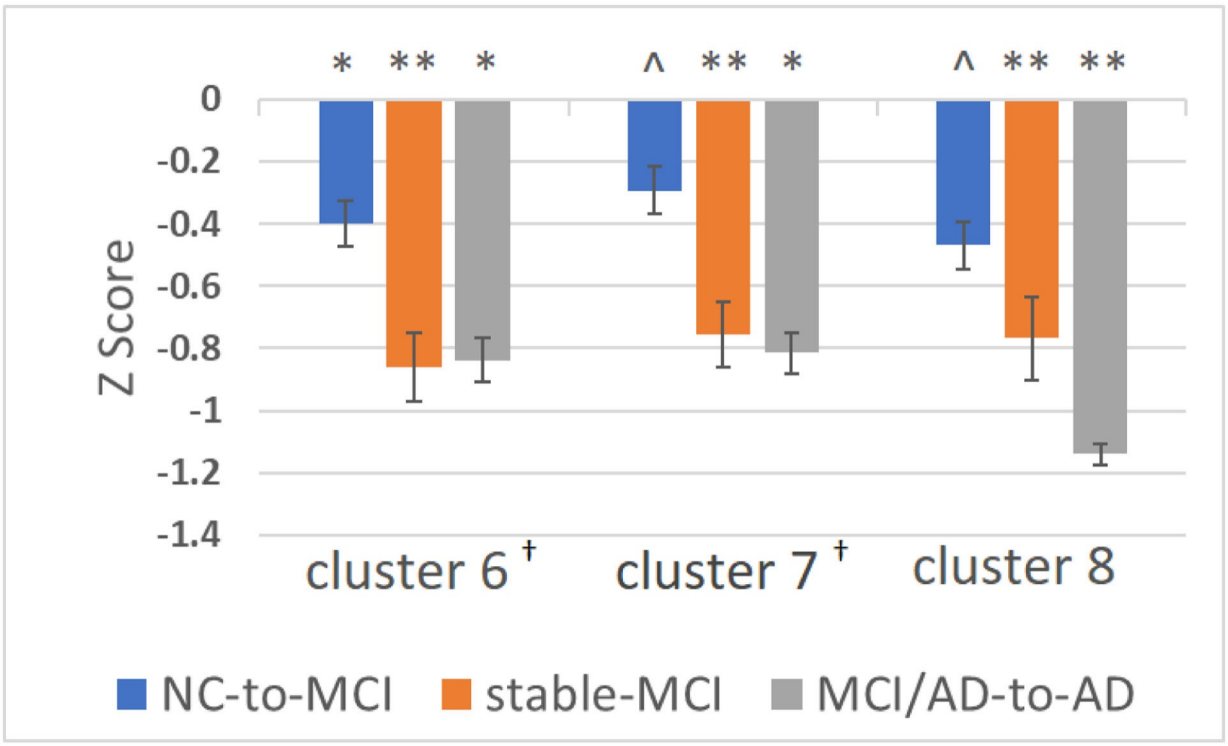

Fig. 6.

Z scores of regional k_{for} changes in the NC-to-MCI, Stable-MCI, and MCI/AD-to-AD groups compared to the stable-NC group. ^, * and ** represent the significance group differences with $0.05 \leq p < 0.1$, $0.01 \leq p < 0.05$, and $p < 0.01$, respectively. Clusters 6–8 are the clusters identified from the voxel-based longitudinal group comparisons of k_{for} changes with voxel-level $p < 0.025$.

Table 1.

Demographic and cognitive scores at baseline and follow-up. The differences between two time points were calculated by subtracting the baseline values from follow-up values.

Baseline (n = 63)				
	NC (n=20)	**MCI (n=18)**	**AD (n=25)**	**P-value**
Age (years)	84.40 ± 4.38	84.40 ± 3.30	84.77 ± 3.01	0.1986
Gender (F, %)	10 (50%)	12 (67%)	20 (80%)	0.1054
3MSE scores†	94.72 ± 3.87 (n' = 17)	91.89 ± 8.54 (n' = 15)	82.70 ± 11.92 (n' = 23)	0.0001

Follow-up (n = 53)					
	Stable NC (n=15)	**NC to MCI (n=12)**	**Stable MCI (n=12)**	**MCI/AD to AD (n=14)**	**P-value**
Baseline age (years)	83.13 ± 3.94	83.45 ± 3.06	85.99 ± 4.05	82.91 ± 3.30	0.7435
Gender (F, %)	9 (60%)	6 (50%)	8 (67%)	9 (64%)	0.8425
Follow-up Time (years)	2.75 ± 1.90	3.08 ± 2.20	2.69 ± 1.81	1.91 ± 1.37	0.4494
Baseline 3MSE scores	95.26 ± 3.67	95.41 ± 4.39	95.62 ± 2.46	86.73 ± 6.96	0.0055
3MSE change†	−0.27 ± 3.77 (n' = 13)	−0.94 ± 2.26 (n' = 9)	−0.05 ± 3.17 (n' = 11)	−3.14 ± 4.65 (n' = 12)	0.2125

†3MSE scores were not completed for all the subjects at the baseline and follow-up studies. The actual number of subjects with the 3MSE scores measured is indicated inside the brackets.

Table 2.

Summary of cluster-level statistics for clusters with significant k_{for} differences among the NC, MCI and AD groups.

Cluster	No. voxels	Peak-t	Peak-t MNI coordinates	GM/WM	Anatomical locations	%Cluster	%Region
1 NC > AD	407	3.78	−28.8 14.0 26.0	WM	Corona radiata [L]	60.69%	13.81%
2 NC > AD	983	3.77	34.0 −8.0 50.0	WM	Corona radiata [R]	28.89%	12.75%
					Superior longitudinal fasciculus [R]	4.07%	4.85%
				GM	Middle frontal [R]	14.04%	2.70%
					Precentral [R]	11.60%	3.37%
					Operculum inferior frontal [R]	3.56%	2.50%
					Inferior triangularis frontal [R]	2.54%	1.16%
3 NC > AD	485	3.77	6.0 −36.0 58.0	WM	Superior longitudinal fasciculus [R]	4.95%	2.91%
				GM	Postcentral [R]	46.19%	5.86%
					Paracentral Lobule[R]	24.74%	14.35%
					Precuneus [R]	7.63%	1.13%
4 MCI >AD	2401	4.97	−14.0 40.0 2.0	WM	Corona radiata [L]	31.57%	42.37%
					Internal capsule [L]	6.16%	12.54%
					External capsule [L]	4.00%	13.87%
					Corpus callosum	3.62%	3.04%
				GM	Anterior cingulum [L]	8.25%	5.93%
					Superior medial frontal [L]	5.58%	4.48%
					Putamen [L]	5.16%	12.29%
					Precentral [L]	2.79%	1.90%
					Insula [L]	2.67%	3.44%
					Superior frontal [L]	2.58%	1.72%
					Middle frontal [L]	2.04%	1.01%
					Supplementary motor area [L]	1.58%	1.77%
5 MCI >AD	2502	4.51	30.0 22.0 10.0	WM	Corona radiata [R]	29.78%	41.95%
					External capsule [R]	7.43%	25.51%
					Superior longitudinal fasciculus [R]	5.64%	17.09%
					Internal capsule [R]	1.84%	3.76%
				GM	Superior frontal [R]	8.83%	5.45%
					Putamen [R]	5.48%	12.88%
					Middle frontal [R]	5.12%	2.51%
					Insula [R]	4.96%	7.01%
					Inferior triangularis frontal [R]	1.44%	1.67%

The Johns Hopkins University (JHU) WM atlas and automated anatomical labeling (AAL) GM atlas were used to label anatomical locations. %Cluster indicates the percentage of each cluster that falls within the defined region, %Region indicates the percentage of each defined region that falls within the cluster. The listed anatomical regions are either "%Cluster" > 1% or "%Region" > 1%.

Table 3.

Summary of cluster-level statistics for clusters with significantly larger k_{for} decreases among the stable-NC, NC-to-MCI, stable-MCI and MCI/AD-to-AD groups. The k_{for} decreases were calculated by subtracting follow-up k_{for} values from baseline values.

Cluster	No. voxels	Peak-t	Peak-t MNI coordinates	GM/ WM	Anatomical locations	%Cluster	%Region
6 stable-MCI > stable-NC	652	3.47	−38.0 −32.0 42.0	WM	Corona radiata [L]	12.58%	5.99%
					Superior longitudinal fasciculus [L]	11.04%	8.83%
				GM	Inferior parietal [L]	16.41%	4.37%
					Postcentral [L]	15.80%	2.65%
7 stable-MCI > stable-NC	435	3.32	26.0 20.0 28.0	WM	Corona radiata [R]	33.79%	8.28%
				GM	Superior frontal [R]	11.49%	1.23%
8 MCI/AD-to-AD > stable-NC	1010	3.73	−20.0 −48.0 24.0	WM	Corpus callosum	24.06%	7.43%
					Superior longitudinal fasciculus [R]	6.34%	7.76%
					Corona radiata [R]	6.24%	7.02%
					Cingulum	4.26%	6.81%
				GM	Precuneus [L]	11.19%	3.20%
					Posterior cingulum[L]	10.79%	4.53%
					Inferior parietal [L]	5.94%	2.45%
					Posterior cingulum[R]	1.58%	4.78%

The Johns Hopkins University (JHU) WM atlas and automated anatomical labeling (AAL) GM atlas were used to label anatomical locations. %Cluster indicates the percentage of each cluster that falls within the defined region, %Region indicates the percentage of each defined region that falls within the cluster. The listed anatomical regions are either “%Cluster” > 1% or “%Region” > 1%.